Precision Agriculture
https://doi.org/10.1007/s11119-020-09746-y

Computational end-to-end and super-resolution methods to improve thermal infrared remote sensing for agriculture

Iftach Klapp[1] · Peretz Yafin[1,2] · Navot Oz[1,3] · Omri Brand[1,4] · Idan Bahat[1,5] · Eitan Goldshtein[1] · Yafit Cohen[1] · Victor Alchanatis[1] · Nir Sochen[4]

Abstract

Increasing global water deficit and demand for yield improvement call for high-resolution monitoring of irrigation, crop water stress, and crops' general condition. To provide high spatial resolution with high-temperature accuracy, remote sensing is conducted at low altitudes using radiometric longwave thermal infrared cameras. However, the radiometric cameras' price, and the low altitude leading to low coverage in a given time, limit the use of radiometric aerial surveys for agricultural needs. This paper presents progress toward solving both limitations using algorithmic and computational imaging methods: stabilizing the readout of low-cost thermal cameras to obtain radiometric data, and improving the latter's low resolution by applying convolutional neural network-based super-resolution. The two methods were merged by an end-to-end algorithm pipeline, providing a large mosaicked image of the field. First, the potential capabilities of a joint estimation method to correct unknown offset and gain were simulated on remotely sensed agricultural data. Comparison to ground-truth measurements showed radiometric accuracy with a root mean square error (RMSE) of 1.3 °C to 1.8 °C. Then, the proposed super-resolution method was demonstrated on experimental and simulated remotely sensed agricultural data. Preliminary experimental results showed 50% improvement in image sharpness relative to bicubic interpolation. The performance of the algorithm was evaluated on 22 simulated cases at $\times$ 2 and $\times$ 4 magnification. Finally, image mosaicking using the proposed pipeline was demonstrated. A mosaicked image composed of sub-images pre-processed by the proposed computational methods resulted in a RMSE in temperature of 0.8 °C, as compared to 8.2 °C without the initial processing.

Keywords Computational imaging · Precision agriculture · Radiometry · Remote sensing and sensor · Super-resolution · Thermography

✉ Iftach Klapp
iftach@volcani.agri.gov.il

Extended author information available on the last page of the article

Published online: 21 September 2020

Introduction

Remote sensing in the visible and near-infrared spectral range relies on solar radiation as the illumination source. The sun may be approximated to a black body (BB) at 5 900 degrees Kelvin (K) that illuminates in the range of 0.2 to 3 μm (Kopeika 1998). Wien's law, which ties the peak radiation wavelength to BB radiation (Holman 1989), suggests that $\lambda_{\max} \times T_{bb} = 2897.6\,\mu\text{m} \times \text{K}$ where T_{bb} is the equivalent BB temperature (K) and λ_{max} is the wavelength of the maximal radiant flux (μm). An ~ 300 K BB radiation can typically approximate plant radiation emission, and thus it radiates mostly at 10 μm (infrared radiation, IR). Empirically, it has been found that the atmosphere can be treated as a cold BB with $T_{bb} = 20$ K (Jones 1994). Atmospheric absorption depends on various characteristics, among them relative humidity and distance to the object; in the spectral range between 8 and 13 μm—the thermal IR spectrum—the atmospheric window is almost clear (Kopeika 1998). In the absence of a significant background radiation source, measurements performed in this atmospheric window (sometimes referred to as second atmospheric window) allow remote monitoring of canopy temperature. Realizing the technical possibility of remotely estimating canopy temperature, thermal imaging has been adopted for many agricultural monitoring tasks, including yield assessment, plant physiology, irrigation level, and leaf water content (Manickavasagan et al. 2005). Indeed, the ability to evaluate "crop water stress" from measurements of canopy temperature has been known for many years (Tanner 1963; Gates 1964; Ehrler 1973). Evaluation of water status by imaging the crop canopy with a focal plane array (FPA) thermal camera has been reported in the literature for, among others, wheat (Tilling et al. 2007), grapevine (Grant et al. 2007), olive (Berni et al. 2009), cotton (Alchanatis et al. 2010), and palm trees (Cohen et al. 2012). The relationship between evaporation and heat exchange has led to the development of methods to estimate gas exchange based on thermography (e.g., Costa et al. 2013). Other studies have shown that thermography can be used for irrigation control (e.g., Petrović et al. 2016). In recent work, thermography was shown to be effective at recognizing wood defects for an assessment of tree health (Vidal and Pitarma 2019).

The United Nations (2017) has estimated a 50% increase in the water required for irrigation by 2050, on top of the increasing global irrigation-water deficit due to global warming and the constant demand for yield improvement, all calling for urgent improvements in irrigation management. In addition, a field's water status is generally variable in the spatial dimension and therefore requires variable irrigation rates. To apply variable-rate irrigation, the field has to be divided into irrigation-management zones.

Thermal IR cameras have low sensor resolution. Low-cost uncooled thermal IR cameras have detector arrays with 384 × 288 pixels or less. High-end cameras are limited to 1 megapixel, which is also considered a low resolution in comparison to cameras in the visible range. When radiometric thermal imaging is performed at high altitude, the width of a row of vines in a vineyard or trees in an orchard is covered by only a few pixels, many of them mixed pixels that are subjected to significant bias in temperature measurements. To provide the required high spatial resolution, radiometric remote sensing is conducted from a relatively low altitude, resulting in low area coverage and high costs. One way to lower costs is to retain high-altitude imaging but improve the spatial resolution using a super-resolution (SR) algorithm.

Uncooled, longwave thermal IR cameras that are well radiometrically calibrated, based on microbolometers, are costly—on the order of 25,000 Euros, preventing routine radiometric surveys in agriculture. To lower the cost of such surveys, so that they can become

common practice, the development of a method that stabilizes the readout of low-cost (~2 000 Euros) uncooled microbolometer thermal cameras is proposed. The latter cameras usually suffer from drift due to thermal environmental loads. The main sources of these loads are solar radiation, air temperature, unstable heat transfer due to changes in convection, solar radiation and ground radiation, and wind loads.

Low-cost uncooled microbolometer cameras

Uncooled microbolometer FPA (UCFPA) technology is characterized by a low price, lower power consumption and small physical dimensions. These cameras are widely used in commercial and military applications (Bhan et al. 2009) and are the most commonly used cameras in thermography (Tempelhahn et al. 2016). Their small dimensions and low weight are a big advantage for agriculture because they can be mounted on a microdrone. Nevertheless, these cameras' sensitivity to environmental conditions affects their readings. Kusnierek and Korsaeth (2014) showed that wind load and irradiance have a significant influence on the analog readings of the UCFPA camera (TAU 320, FLIR, USA). Drift in the FPA due to environmental load limits its ability to acquire informative radiometric images. Thus, stabilizing the camera's readout by calibrating its response is an important challenge. The FPA camera image is a function of its optics and its detector's response; image formation, in lexicographic form, is:

$$\mathbf{y}(T) = \left[\mathbf{G_1}(T)\right][\mathbf{A}]\mathbf{x} + \mathbf{d}(T) + \mathbf{n} \tag{1}$$

where **[A]** is the point-spread function (PSF) matrix representing the optical blur, **y** is the FPA image, **x** is the object's radiation, **[G]** is the gain matrix, **n** is the noise, and (**x,d,y,n**) are vectors in lexicographic form. The gain and offset depend on FPA temperature and changes in environmental temperature (Nugent and Shaw 2014). These relatively rapid changes require constant calibration against a BB (Tempelhahn et al. 2016). Whereas gain calibration is relatively simple, being a linear function of the FPA's temperature, offset calibration is more complex.

Super-resolution (SR)

With any camera, higher field coverage results in decreased image resolution, and vice versa. SR is a collection of methods that exploit information redundancy and prior knowledge to improve the spatial resolution of a given image. When possible, such improvement can eliminate the tradeoff between field of view (FOV) and resolution; this, in turn, enables faster flights at higher altitudes, potentially lowering the aerial survey's cost. There are a few main approaches to SR imaging. Elad and Feuer (1997) and Farsiu et al. (2004) showed that known image formation enables using a sequence of non-identical images to produce an image with improved resolution. In a recent work, Mandanici et al. (2019) showed that using rotated and translated images can improve the spatial resolution by a factor of 4. Another SR methodology is single-image SR. The SR of a single image is a convolutional neural network (CNN) based on a learning scheme, which is trained to learn the upscaling function from a low-resolution replica of an image to its high-resolution replica (Dong et al. 2014; Kim et al. 2016; Rivenson et al. 2017). Upon input of a low-resolution image, the system output is an estimated high-resolution image; the output of this SR process is denoted I_{SR}. Previous work (Klapp et al. 2019) has shown that a SR schema for

microscopy proposed by Rivenson et al. (2017) can, after some modification, be used for SR of visible remotely sensed images, such as visible images of cotton flowers.

One can see the SR process as a learning operation trained to transfer gradient statistics in low resolution to statistics in higher resolution (Sun et al. 2008). However, compared to visible images, the IR image consists of a single channel and its gradients may differ. Reduction to a single channel also affects any possible correlation between channels, as shown in the multispectral case (Zhou et al. 2016). In addition, bearing in mind the cost issues and the requirement for a portable solution, an IR network for agricultural use should be a low-cost solution in terms of computation as well.

The objectives of this work were: (1) to improve the resolution of low-cost thermal IR cameras; (2) to decrease the drift in the readings of low-cost thermal IR cameras; (3) to develop a single pipeline to perform objectives 1 and 2, for environmental scenarios in remote-sensing agricultural monitoring tasks. This paper presents new results on the algorithmic and computational imaging methods used to achieve these objectives.

A novel end-to-end solution is suggested that addresses the need to lower the cost of IR aerial radiometric surveys for agriculture. This effort was divided into two complementary tasks that ended with engaging the resulting method in a unified pipeline algorithm. This paper extends the findings of a previous work (Klapp et al. 2019). First, extensive simulation results of stabilizing the readout of a low-cost IR camera when both offset and gain are unknown are presented and discussed with respect to typical remotely sensed agricultural scenarios. Then preliminary experimental results for SR imaging followed by extensive simulated results for typical IR remote-sensing in agriculture are presented and discussed. Finally, conceptual results link these two approaches, showing the benefits of the overall approach and its potential contribution to mosaicking over an agricultural field, showing a mosaicked image that is an order of magnitude more accurate than that acquired by conventional methods.

Materials and methods

Data acquisition

To investigate the accuracy of the presented method in an agricultural scenario, data of three different crops, acquired from three commercial plots were used. *Vineyard* a highly variable 2.4 ha Vitis vinifera cv. Cabernet Sauvignon vineyard, established in Mevo-Beitar (31.729522 ^{o}N; 35.1031 ^{o}E) in the Judean hills region in Israel. Vines were planted in 2011 in a northwest to southeast direction with a vine and row spacing of 1.5 m and 3.0 m, respectively. *Peach orchard* a 0.4 ha peach orchard located in an area of slightly hilly terrain in the Upper Galilee (33.012322 °N; 35.606314 °E). The orchard's lithology is primarily alluvium composed of clay, volcanic gravel, and chalk. The slope of the field is 5%. The orchard was planted in 2007 with a late-harvesting peach variety, with 2.6 m and 5 m between trees and rows, respectively, and rows running from northwest to southeast. *Cotton* a 15 ha cotton field, located in the southeastern coastal plain of Israel (31.833792 °N; 34.710056 °E), belonging to Bnei-Darom and Kibbutz Yavne. Most of these were planted with Gossypium barbadense L. cv. Pima and a G. hirsutum × G. barbadense hybrid ('Akalpi') in 0.97-m spaced rows. Measurements at these commercial plots were performed through the spring at midday on several occasions. *Single*

trees palm and oak trees were measured at midday at the Agricultural Engineering Institute campus of the Volcani Center (32.003744 °N; 34.816778 °E) on 25 Nov 2019.

For IR image acquisition in an agricultural field, a FLIR A655Sc camera was used. This is an uncooled microbolometer, 640×480 pixels, sensitive to radiation in the range of 7.5–14.0 µm, equipped with a lens with a focal length of 24 mm (https://www.flir.com/products/a655sc/). The camera was mounted on a light airplane flown at an altitude of 500 m above ground level, resulting in a ground sampling distance of 0.35 m. The emissivity of the plants was set to 0.98. Images were acquired at midday under clear sky conditions. A series of thermal images were acquired at a frame rate of 6 frames per second and stored as one file (*.SEQ format). At the time of the imaging, the temperature range in the vineyard images was 24.48 °C to 70.29 °C, in the cotton field images it was 29.36 °C to 69.15 °C, and in the peach orchard it was 31.09 °C to 71.19 °C. Each gray level represents 0.01 °C. The algorithms presented below were fed with a sequence of images acquired by post-processing the SEQ video saved in.jpg format using FLIR Tools software. Images of the singles trees were acquired using a low-cost uncooled thermal camera (Opgal Therm-APP TH, https://www.opgal.com/products/therm-app-th/) mounted on a tripod, and operated by cellular phone application. The temperature range of the images taken by the Therm-APP TH was − 10 °C to 45 °C with 16-bit output. The images were acquired from a distance of 200 m. The emissivity of the objects was set to 0.98. Image acquisition was performed at midday under clear sky conditions.

Root mean square error (RMSE)

To evaluate the quality of the restored images, differences between original and reconstructed images were computed pixel by pixel, and the RMSE was used as an indicator of algorithm performance:

$$RMSE = \frac{1}{V \cdot U}\sqrt{\sum_{V}\sum_{U}\left(\mathbf{I_e}(i,j) - \mathbf{I_{gth}}(i,j)\right)^2}, \text{ [gray level]} \tag{2}$$

where $U \times V$ is the image size, $\mathbf{I_e}$ is the estimated image, and $\mathbf{I_{gth}}$ is the ground-truth image. When evaluating the restoration of radiometric values, $\mathbf{I_e}$ is the estimated image, while $\mathbf{I_{gth}}$ is the ground-truth image before corruption by the unknown gain and offset. When evaluating SR, $\mathbf{I_e}$ is the estimated high-resolution image, and $\mathbf{I_{gth}}$ is the ground-truth high-resolution image.

Evaluating the performance of the proposed CNN

The proposed CNNSR algorithm relies on CNN architecture. The learning process of the CNNSR relies on learning the transformation between low-resolution and high-resolution replicates of the objects. This transformation depends on the camera's behavior (i.e., the optical response and blur), temperature range, and target spatial structure.

The SR performance was evaluated by the peak signal-to-noise ratio (PSNR) as follows:

$$PSNR = 20 \cdot \log_{10}\left[\frac{\left(2^N - 1\right)}{RMSE}\right], \text{ [db]} \tag{3}$$

where N is the grayscale depth. PSNR expresses the ratio between the dynamic range of the image ($2^N - 1$ grayscale levels) and the restoration error in grayscale. PSNR values increase with decreasing restoration error and are commonly presented in decibels [db].

Another way to compare images is by the intersection of their histograms, H1 (Jia et al. 2006), such that:

$$H1 = \sum_i \min(h_1(i), h_2(i)) \tag{4}$$

where h_1 and h_2 are the normalized histograms of the compared images, and i is the bin number. The more similar the histograms are, the closer the value of H1 to 1.

Naïve mosaicking method

Assuming a best-case scenario in which frame perspective is perfectly corrected and the registration between sequential frames is perfectly known, one can represent the mosaicking as the following process:

$$\begin{pmatrix} \mathbf{y_1} \\ \mathbf{y_2} \\ \\ \mathbf{y_n} \end{pmatrix} = \begin{pmatrix} \mathbf{C_1} \\ \mathbf{C_2} \\ \\ \mathbf{C_n} \end{pmatrix} \mathbf{x} \tag{5}$$

where $\mathbf{x}$ is the image of the overall FOV in lexicographic form, $\mathbf{C_i}$'s are the cropping matrices and $\{\mathbf{y_i}\}$ are the cropped images in lexicographic form. In reality, $\mathbf{x}$ needs to be estimated by mosaicking a series of partially overlapping images which may be frames of a video taken over the course of an aerial survey. The $\mathbf{C_i}$ matrices are estimated by a registration process, $\mathbf{C_i}$ is an $N \times M$ rectangular matrix, where N is the length of $\mathbf{y_i}$ and M is the length of x; typically, $M >> N$. For simplicity, the registration results are assumed to be an integer step. A typical form of C_i under these assumptions is:

$$\mathbf{C_i} = \begin{pmatrix} 0 & 1 & 0 & \cdots & & 0 \\ & 0 & \ddots & 0 & \cdots & \\ & & 0 & 1 & 0 & \cdots \\ \vdots & & & \ddots & \ddots & \ddots & \vdots \end{pmatrix}_{N \times M} \tag{6}$$

It should be noted that some of the diagonal values might be zero due to the lexicographic transformation from the 2D image to a 1D vector. Let $\mathbf{y} = \begin{pmatrix} \mathbf{y_1} & \mathbf{y_2} & \cdots & \mathbf{y_n} \end{pmatrix}^T$, $[\mathbf{C}]^\mathbf{T} = \begin{pmatrix} \mathbf{C_1} & \mathbf{C_2} & \cdots & \mathbf{C_n} \end{pmatrix}^\mathbf{T}$, a compact form of the least-square representation of the problem and an estimation of the mosaic image is:

$$[\mathbf{C}]^\mathbf{T}\mathbf{y} = [\mathbf{C}]^\mathbf{T}[\mathbf{C}]\mathbf{x} \Rightarrow \mathbf{x} = \left([\mathbf{C}]^\mathbf{T}[\mathbf{C}]\right)^{-1}[\mathbf{C}]^\mathbf{T}\mathbf{y} \tag{7}$$

Stabilizing the readout of the low-cost uncooled thermal FPA

This section provides a brief introduction to a previously suggested method for estimating radiometric values from a series of images taken by a thermal camera that suffers from unknown drift in offset and gain, termed "joint estimation method". For complete details, the reader is referred to Klapp et al. (2017) and Papini et al. (2018).

The image formation equation is given in Eq. (1). If the parameters of the image formation, **[A]**, **[G]** and **d**, are known, given an image y, one can solve an inverse problem of Eq. (1) to restore the radiometric values of the object x such that:

$$\mathbf{x_{LS}} = \left[([\mathbf{G}][\mathbf{A}])^{\mathbf{T}}([\mathbf{G}]\cdot[\mathbf{A}])\right]^{-1}([\mathbf{G}]\cdot[\mathbf{A}])^{\mathbf{T}}(\mathbf{y}-\mathbf{d}) \tag{8}$$

where $\mathbf{x_{LS}}$ is the least-square solution. However, in environmental scenarios, the low-cost thermal cameras tend to suffer from drift in offset **d** and gain **[G]**, such that the solution of Eq. (1) becomes an indeterminate equation. In previous work, it was shown that a way to make this situation solvable is to add more equations to the problem. This was done by using a sequence of pairs of sharp and defocused images. While both gain and offset drift with temperature, the gain is easier to calibrate against a BB. Starting with the case in which the gain is calibrated (Klapp et al. 2017), both vectors **y** and matrix **[G]** are known. This leaves Eq. (1) with both **x** and **d** ($2 \times N$ values) unknown. Since Eq. (1) is a linear system composed of N equations, a list of N additional equations is required to solve it. To gain the additional N known equations, it was suggested to measure a pair of images for each object (focused and defocused), $\mathbf{y_1}$ and $\mathbf{y_2}$, respectively. Thus, two sequential images were taken with two known and different PSF matrices, $[\mathbf{A_1}]$ and $[\mathbf{A_2}]$. Since the camera integration time is much faster than changes in thermal load, the gain and offset can be assumed to not change and therefore, formation of the images is:

$$\begin{aligned} \mathbf{y_1}(T) &= [\mathbf{G}]\left[\mathbf{A_1}\right]\mathbf{x} + \mathbf{d}(T) + \mathbf{n_1} \\ \mathbf{y_2}(T) &= [\mathbf{G}]\left[\mathbf{A_2}\right]\mathbf{x} + \mathbf{d}(T) + \mathbf{n_2} \\ \left[\mathbf{A_1}\right] &\neq \left[\mathbf{A_2}\right] \end{aligned} \tag{9}$$

where $\mathbf{y_1}$ and $\mathbf{y_2}$ are sharp and blurred images of the same object x. The use of two blur levels creates the required difference between the equations. The unknown offset is estimated by substituting one equation into the other. The estimation for the offset is (Klapp et al. 2017):

$$\mathbf{d}(T) = inv\left\{[\mathbf{G}]\left[\mathbf{A_1}\right]inv\left\{[\mathbf{G}]\left[\mathbf{A_2}\right]\right\} - [\mathbf{I}]\right\}\left([\mathbf{G}]\cdot\left[\mathbf{A_1}\right]inv\left\{[\mathbf{G}]\cdot\left[\mathbf{A_2}\right]\right\}\mathbf{y_2} - \mathbf{y_1}\right) \tag{10}$$

The inverse problem of image formation is solved by substituting Eq. (10) into the image formation equation (Eq. 1). The resultant estimator for object radiation is:

$$\mathbf{x_{LS}} = inv\left\{\left[\mathbf{G_2}\right]\left[\mathbf{A_2}\right]\right\}\left(\mathbf{y_2} - \mathbf{d}(T)\right) \tag{11}$$

where the *inv{}* operation refers to a general inverse operation. For a detailed account of the proposed algorithm, see Klapp et al. (2017).

Since in reality, both gain and offset drift, to solve the inverse problem one must tackle the situation in which both $[G]$ and d are unknown. In that case, there are an additional N unknown parameters associated with the gain, and therefore measuring one pair of images is not enough. To obtain a sufficient number of equations, it was suggested that at least one additional sharp and blurred pair of a different object, x^*, with a different image, y^*, be introduced (Papini et al. 2018), such that:

$$\begin{aligned} [\mathbf{G}]\left[\mathbf{A_1}\right]inv\left\{[\mathbf{G}]\left[\mathbf{A_2}\right]\right\}\mathbf{d} - \mathbf{d} &= [\mathbf{G}]\left[\mathbf{A_1}\right]inv\left\{[\mathbf{G}]\left[\mathbf{A_2}\right]\right\}\mathbf{y_2} - \mathbf{y_1} \\ [\mathbf{G}]\left[\mathbf{A_1}\right]inv\left\{[\mathbf{G}]\left[\mathbf{A_2}\right]\right\}\mathbf{d} - \mathbf{d} &= [\mathbf{G}]\left[\mathbf{A_1}\right]inv\left\{[\mathbf{G}]\left[\mathbf{A_2}\right]\right\}\mathbf{y_2}^* - \mathbf{y_1}^* \end{aligned} \tag{12}$$

This system poses two additional obstacles. The first is the additive noise (n), which changes randomly from image to image. This is overcome by using M number of pairs. Since the unknown gain $[G]$ and unknown objects multiply one another, this simplification enables determining their solution up to a scale (Papini et al. 2018). A unique solution is determined by using prior knowledge of solution behavior (Papini et al. 2018). The system is solved as the minimization of a cost function:

$$S\left([\mathbf{G}],\mathbf{d},\{\mathbf{x_i}\}\right)=\sum_{i=1}^{M}\sum_{j=1}^{2}\left\|\mathbf{y_{i,j}}-[\mathbf{G}]\cdot\left([\mathbf{A_j}]\mathbf{x_i}\right)-\mathbf{d}\right\|_2^2 \tag{13}$$

where $\{\mathbf{x_i}\}$ is a series of N different objects. Minimization of $S\left([\mathbf{G}],\mathbf{d},\{\mathbf{x_i}\}\right)$ is a demanding computational task that should be done efficiently. The system can be reorganized to fit the least-square QR algorithm (LSQR 2018), solver. Since $[\mathbf{G}],\mathbf{d},\{\mathbf{x_i}\}$ are not known, the solution is reached iteratively (Papini et al. 2018).

Single-image SR for IR image by CNN

The network proposed in Oz et al. (2020) was adopted in this work. A simplified schema of the proposed CNNSR network is depicted in Fig. 1. The CNN decomposes the low-resolution image, I_{LR}, into a few channels, each of which is a filter.

The output of each layer is concatenated with the outputs of all previous layers. The input is interpolated and concatenated to the output of the shuffle block. The network output is the SR image, denoted I_{SR}. The data are composed of bicubic interpolation results and high-resolution features. Initially, the system is trained for close-range imaging (1–3 m) with a low-cost uncooled thermal IR camera. For the sake of saving on computational effort, most computation operations of the network are done in the low-resolution domain. This design resulted in high-level restoration, with PSNR similar to the state-of-the-art VDSR deep-learning net (Kim et al. 2016) and 28 times better computational efficiency. The compact algorithm is critical for processing the big data that are typical in agricultural imagery.

End-to-end computational approach

Agricultural fields are very wide targets that cover tens to hundreds of hectares or more. Aerial surveys of fields are generally done in strips composed of many images (frames);

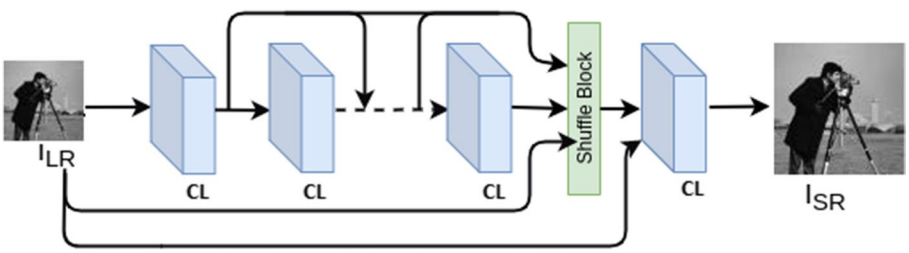

Fig. 1 Low-computation convolutional neural network for super-resolution (CNNSR) of low-cost uncooled thermal IR images. I_{LR} is the low-resolution image input, I_{SR} is the super-resolution image output. The blocks of the convolution layers are denoted CL

depending on flight height, each image covers only a portion of the field, so that a complete view of variability in the field requires mosaicking for a bigger image. In a standard mosaicking algorithm, each pixel of the mosaic image is an interpolation result of several pixels provided by different frames that are partially overlapping in their FOV, which essentially should have correct radiometric values and be well registered. In previous work with mosaicking of visible and radiometric thermal IR images, a 70 to 80% overlap between images was used. Registration is a result of minimizing cost functions, which looks for the similarity between overlapped frames. Thus, in principle, space-variant errors in gain and offset may affect registration efficiency due to their effect on similarity. On the other hand, correction and resolution enhancement by SR will contribute to the mosaicking process, and an end-to-end process is therefore suggested, composed of the following steps:

(1) Radiometric correction
(2) Super-resolution (SR)
(3) Mosaicking.

Results and discussion

Stabilizing the readout of a low-cost uncooled thermal FPA

In this section, the efficiency of the "joint estimation method" to recover radiometric data of remote-sensing agriculture images is investigated. Simulation results are presented for thermal images taken consecutively by a thermal camera subjected to unknown drift in offset and gain. Following the method, a series of objects is jointly estimated; each object was imaged twice, the first image sharp and the second image blurred, with a defocus level equal to one wavelength of 10 μm.

It was assumed that after the initial standard bad-pixel correction and two-point correction, both offset and gain drift to an unknown value. To adopt a realistic spatial distribution in the simulations, a model resembling gain and offset was used; the gain and offset values were calibrated to previously measured experimental values, such as those measured by Tempelhahn et al. (2016):

$$\begin{aligned} G(r) &= \left[(x-0.3\cdot W)^2+(x-0.7\cdot H)^2\right]/[(W\cdot H+0.3)] \\ d(r) &= 6.25\cdot\left(\sigma_x\cdot\left[\left((x-0.5\cdot W)^4+(y-0.4\cdot H)^4\right)\right]/\left[\left(0.4\cdot H^2\cdot W^2\right)-0.3\right]-346.86\right), \\ r &= \sqrt{x^2+y^2}. \end{aligned} \tag{14}$$

The offset has a typical proportion relative to the radiometric values. Gain values are close to 1. To enforce this proportion in the present case, the offset expressions are in proportion to the ensemble standard deviation. W and H are the width and height of the imager FOV. The spatial distribution of the gain and offset is presented in Fig. 2a and b, respectively. White Gaussian noise with a signal-to-noise ratio of 1000 was added to the images.

Below, the restoration results are presented for the three different agricultural fields. The restoration was done jointly using N = 9 images of each field. The series of defocused/focused pairs, and ground-truth and restoration results for the vineyard, cotton field, and peach orchard are presented in Figs. 3, 4 and 5, respectively. Enlarged replicas images of

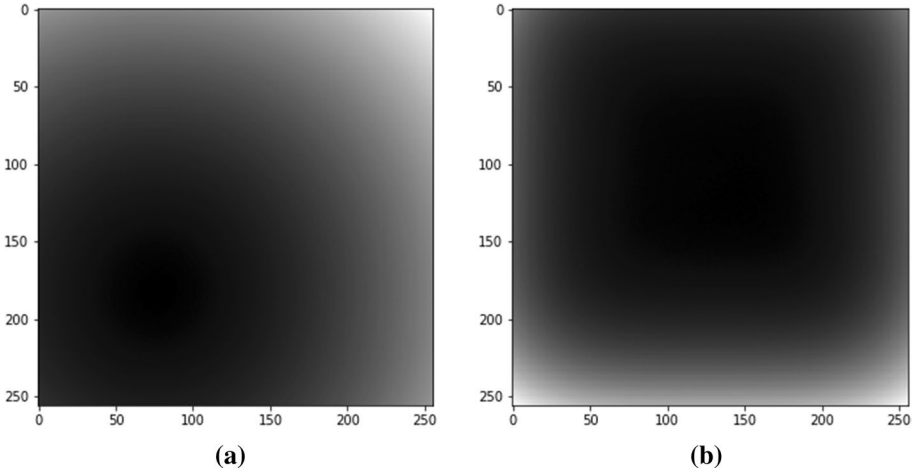

Fig. 2 Unknown gain and offset, focal plane array (FPA) composed of 256 × 256 pixels. **a** Spatial gain function. **b** Spatial offset function

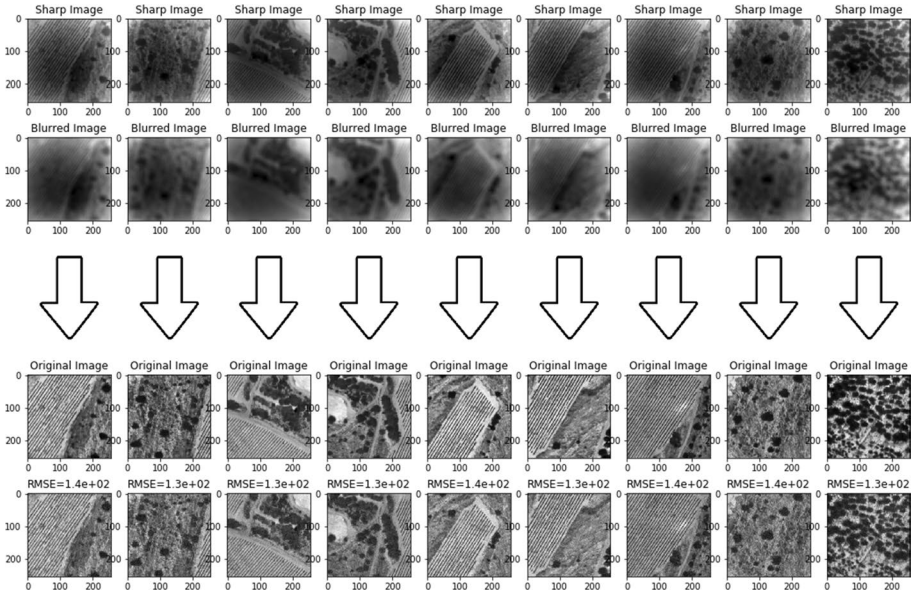

Fig. 3 Results of joint estimation of N = 9 vineyard radiometric images given pairs of focused and defocused thermal images taken with a thermal camera with unknown offset and gain. The gain, offset and N = 9 radiometric images for each thermal pair were jointly estimated. Source images were taken with a FLIR A655Sc camera. Ground sampling distance was 35 cm, sub-image area is 90.6×90.6 m^2

the first two results (from the left) for each of the crops are presented in Figs. 6, 7 and 8, respectively.

Figures 3, 4 and 5 are organized as follows. The nine distracted pairs of images are given one below the other in rows 1 and 2, sharp and blurred, respectively. The ground-truth

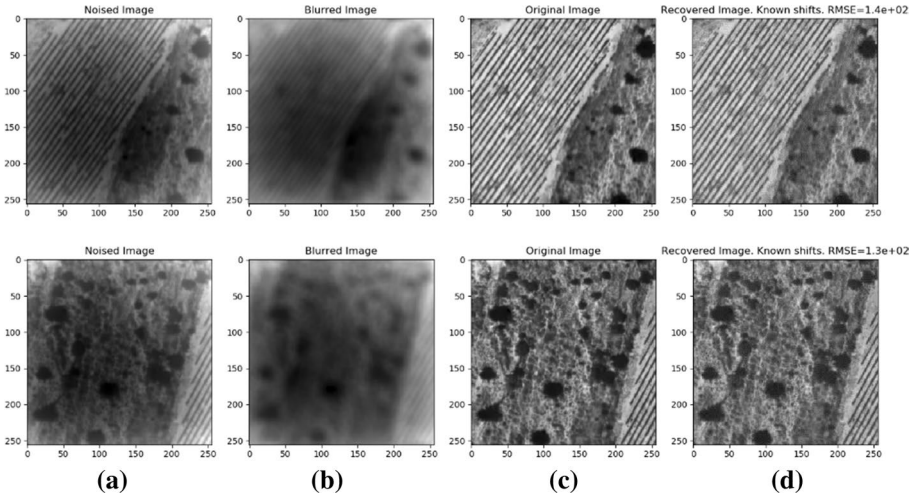

Fig. 4 Three enlarged vineyard examples. Columns from left to right: **a** sharp image with unknown offset and gain; **b** blurred image with unknown offset and gain; **c** ground-truth image; **d** restored image. Source images were taken with a FLIR A655Sc camera. Ground spatial distance was 35 cm, sub-image area is 90.6 × 90.6 m^2

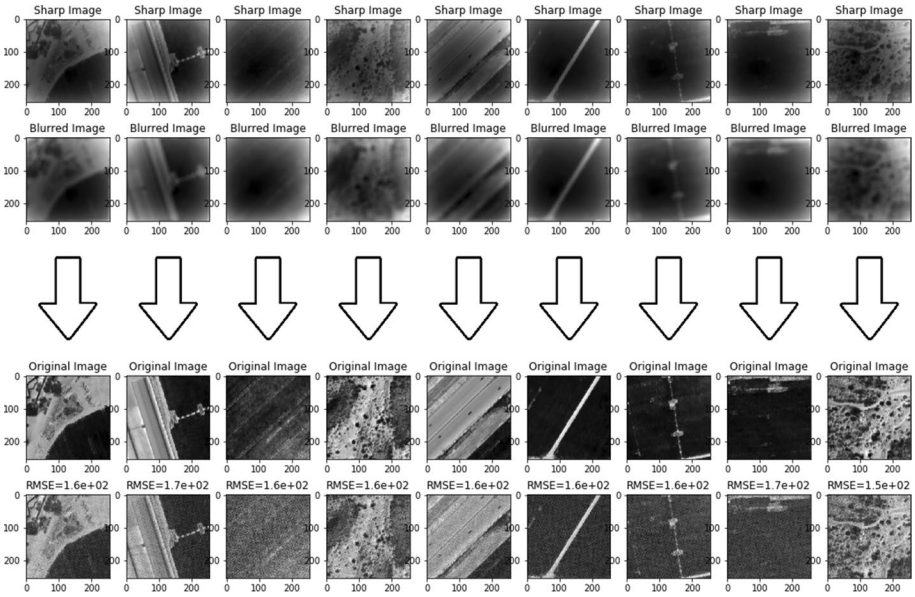

Fig. 5 Results of joint estimation of N = 9 cotton field radiometric images given pairs of focused and defocused thermal images taken with a thermal camera with unknown offset and gain. The gain, offset and N = 9 radiometric images for each thermal pair were jointly estimated. Source images were taken with a FLIR A655Sc camera. Ground sampling distance was 35 cm, sub-image area is 90.6 × 90.6 m^2

object is presented in row 3 and the restored object is presented in row 4. The RMSE in gray level in the 16-bit range is printed above each restoration; the equivalent temperature in degrees Celsius is 1/100 of this numerical value (e.g., a gray level of 1 510 is 15.10 °C).

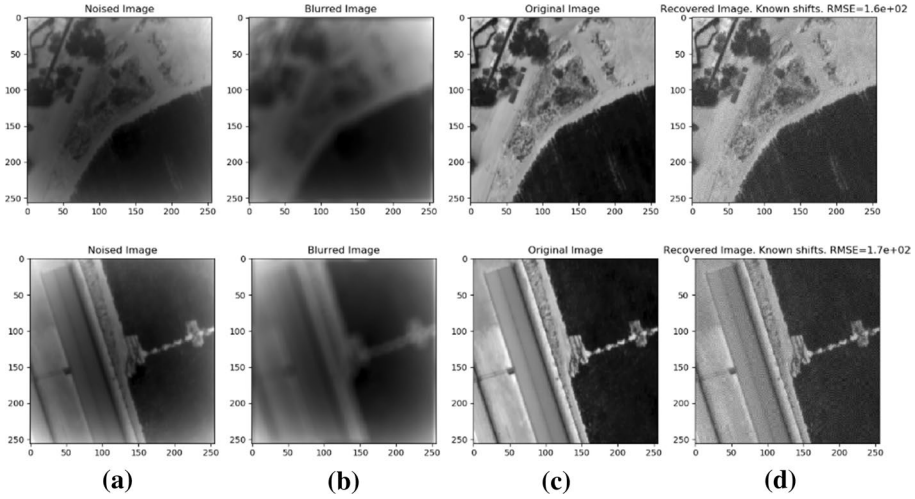

Fig. 6 Three enlarged cotton field examples. Columns from left to right: **a** sharp image with unknown offset and gain; **b** blurred image with unknown offset and gain; **c** ground-truth image; **d** restored image. Source images were taken with a FLIR A655Sc camera. Ground sampling distance was 35 cm, sub-image area is 90.6×90.6 m^2

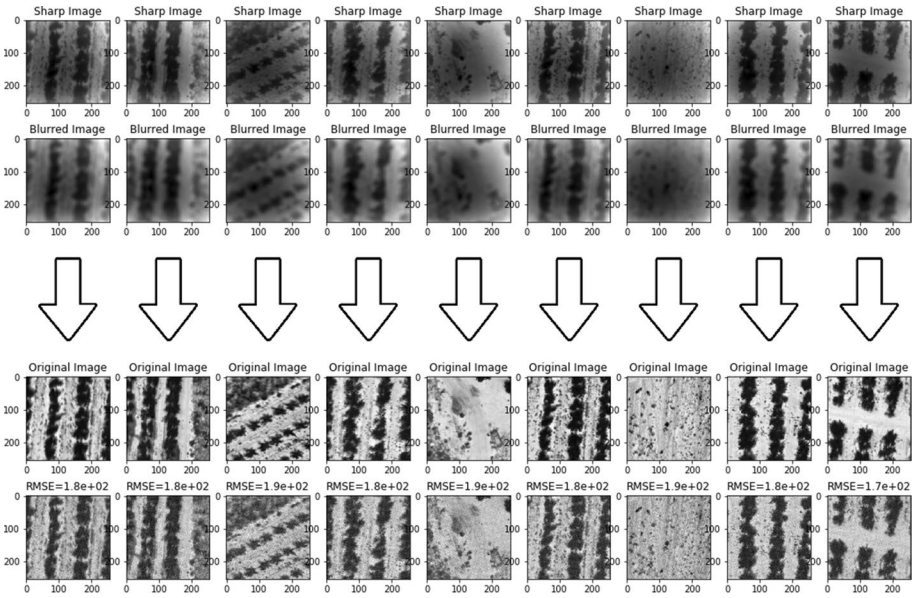

Fig. 7 Results of joint estimation of N = 9 peach orchard radiometric images given pairs of focused and defocused thermal images taken with a thermal camera with unknown offset and gain. The gain, offset and N = 9 radiometric images for each thermal pair were jointly estimated. Source images were taken with FLIR A655Sc camera. Ground sampling distance was 35 cm, sub-image area is 90.6×90.6 m^2

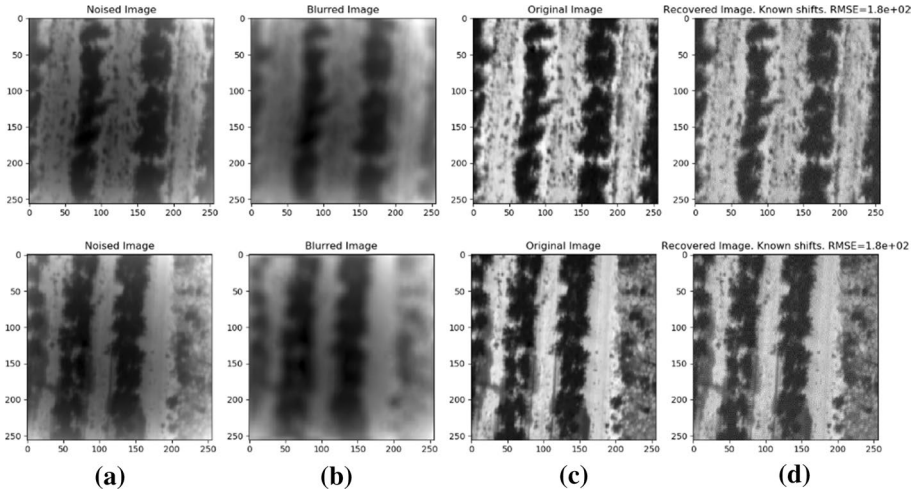

Fig. 8 Three enlarged peach orchard examples. Columns from left to right: **a** sharp image with unknown offset and gain; **b** blurred image with unknown offset and gain; **c** ground-truth image; **d** restored image. Source images were taken with a FLIR A655Sc camera. Ground spatial distance was 35 cm, sub-image area is 90.6×90.6 m^2

Figures 6, 7 and 8 are organized such that the enlarged images are placed one above the other, from left to right: the first column (a) is the sharp image with unknown offset and gain; the second column (b) is the blurred image with unknown offset and gain; the third column (c) is the ground truth; the fourth column (d) is the restored image.

Comparing the restored image to the ground-truth image, the RMSE of the vineyard was in the range of 1.3 °C to 1.4 °C, for the cotton field, 1.5 °C to 1.6 °C, and for the peach orchard, 1.7 °C to 1.8 °C, all in an acceptable range.

SR for IR by CNN: preliminary experimental results

The network was initially trained on agricultural images taken at short-range with a low-cost uncooled thermal camera (Opgal Therm-APP TH). Preliminary results for remotely sensed images of palm and oak trees are presented. The images of the palm trees were measured horizontally from 200 m by the Therm-App TH (Fig. 9a). Using the CNNSR algorithms, the image was processed without any additional training. The CNNSR was trained for typical hot backgrounds, such as the ground in the growing season and vegetation in Israel, and thus to avoid the negative values associated with the sky sub-zero temperature values replaced by zero values before the processing.

For the sake of demonstration, one treetop was chosen as a region of interest (ROI), labeled with a red box in Fig. 9a. The ROI and processing results are presented in Fig. 9b–d: Fig. 9b is the ROI; Fig. 9c is the × 4 result of the bicubic interpolation of the measurement; Fig. 9d is the × 4 CNNSR result. A second preliminary example was the image of an oak tree (Fig. 10a). To demonstrate the method, an arbitrary ROI was chosen (labeled with a red box). The ROI and processing results are presented in Fig. 10b–d. For the sake of simplicity, the figure order is identical to that in Fig. 9.

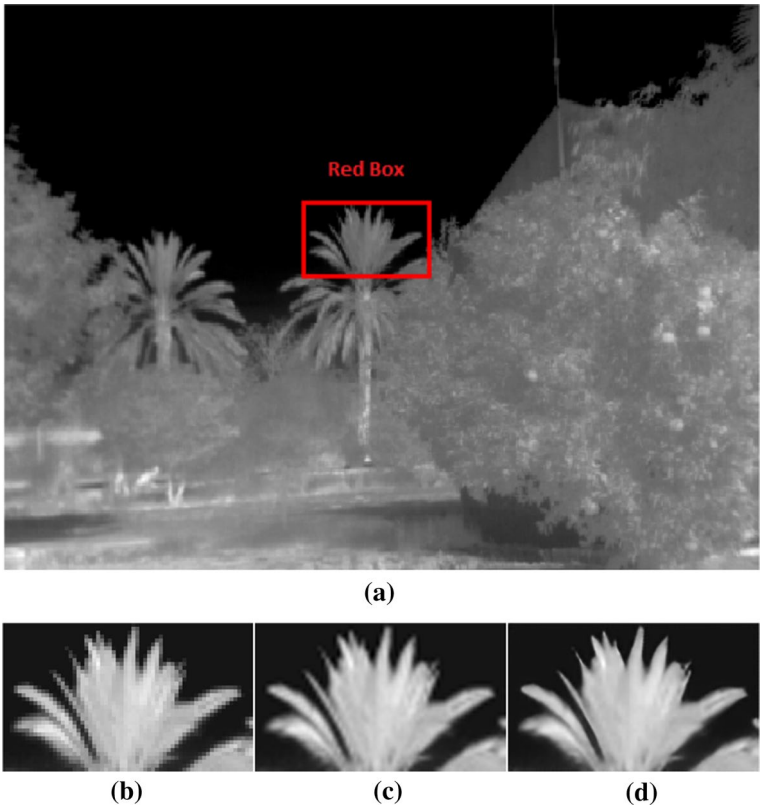

Fig. 9 Palm trees imaged from 200 m, taken with a Therm-App TH camera. **a** General view. **b** ROI in the red box in panel (a) contains the top of one of the trees. **c** 4× result of the bicubic interpolation of the ROI. **d** 4× CNNSR result of the ROI

Observing the results in Figs. 9c, d and 10c, d, the CNNSR (9d and 10d) outperformed the interpolation (9c and 9d) in that the details are significantly sharper. The discontinuity in the tree/sky edges may be treated as a step response. Thus, by differentiating these edges one may evaluate the "smear" kernel representing the bicubic and CNNSR restoration sharpness. Investigating the differentiation results on the two images (not shown here), the full-width half maximum (FWHM) of the bicubic smear is significantly wider, with typical FWHM values of 6 pixels for the bicubic and 4 pixels for the CNNSR.

SR for IR by CNN: accuracy analysis

For the sake of a preliminary quantitative evaluation of CNNSR performance on remotely sensed agricultural data, 11 remote-sensing images were examined at two magnifications, × 2 and × 4. The ground-truth image taken by the FLIR A655Sc was downsampled × 2 and × 4 fold. The resulting image was considered a low-resolution replica of the original image. Using bicubic interpolation and the proposed CNNSR method, the low-resolution

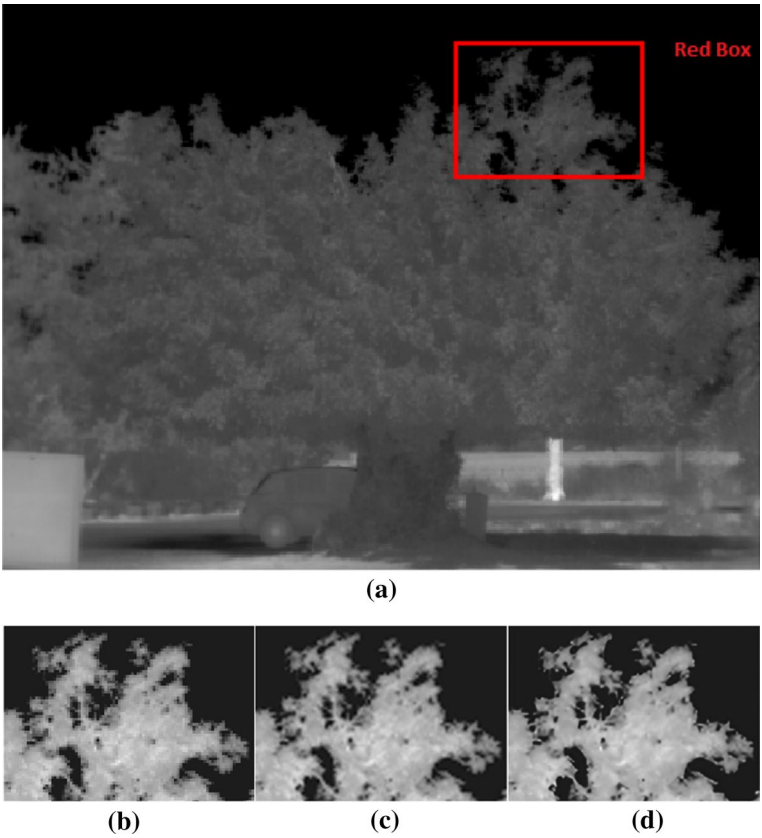

Fig. 10 Oak tree measured from 40 m away taken with a Therm-App TH camera. **a** General view. **b** ROI in the red box in panel (a), contains part of the tree's top. **c** × 4 result of the bicubic interpolation of the measurement. **d** × 4 CNNSR result

image was scaled up. The quality of this upscaling was measured relative to the ground-truth image, and a detailed account of the PSNR results for the tested examples is presented in Table 1.

Observing the results on this limited dataset compared to the alternative bicubic interpolation shows an advantage of 1.8 db in the PSNR score for the × 2 CNNSR, whereas for the × 4 CNNSR, a significant advantage was only seen in the vineyard images.

High resolution is always desirable. However, in agriculture, the aim is not to obtain a nice image, but an informative one. Normally, the canopy temperature is much more important than the ground temperature. When rows are narrow, it is easy to find clean ground pixels to correctly estimate ground resolution, where most of the canopy's pixels are mixed due to the image resolution. In this case, upscaling quality should be evaluated in the ROIs containing important information. The results of the vineyard images upscaled with CNNSR and bicubic interpolation are presented in Fig. 11.

The ground-truth image (Fig. 11d) was taken from an altitude of 500 m, and downscaling by a factor of 4 mimics imaging from 2 km (Fig. 11a), resulting in highly undersampled rows with a high rate of mixed pixels. Observing the restoration results, while the

Table 1 Overall PSNR (db) results for CNNSR (SR) vs. bicubic interpolation (bic)

	× 4		× 2		
PSNR_SR	PSNR_bic	PSNR_SR	PSNR_bic	Name	Crop
35.7	36.4	42.6	40.7	0_full	Cotton
33.5	33.8	39.5	37.8	1_full	Cotton
30.3	29.2	36.3	34.6	0_full	Vineyard
30.6	28.3	34.8	32.9	1_full	Vineyard
30.2	29.1	35.7	34.0	2_full	Vineyard
29.6	27.7	34.6	33.1	3_full	Vineyard
33.3	33.8	40.1	38.4	0_full	Peach
28.5	29.4	35.8	33.9	1_full	Peach
33.0	33.8	40.3	38.3	2_full	Peach
30.0	30.7	36.7	34.9	3_full	Peach
31.5	32.2	38.2	36.4	4_full	Peach
31.5	31.3	37.7	35.9		Average

PSNR peak signal-to-noise ratio, *CNNSR* convolution neural network super-resolution

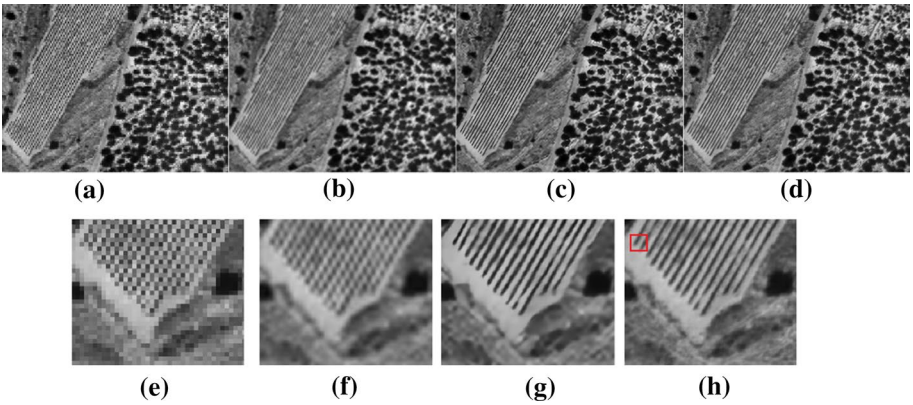

Fig. 11 Vineyard image. **a** Low-resolution image downsampled by a factor of 4. **b** Bicubic upsampling × 4 of the low resolution image (**a**). **c** Convolution neural network super-resolution (CNNSR) algorithm results of processing image (**a**) by a factor of 4. **d** Ground-truth image. **e** Zoomed-in image of (**a**). **f** Zoomed-in image of (**b**). **g** Zoomed-in image of (**c**). **h** Zoomed-in image of (**d**)

bicubic interpolation (Fig. 11b) is only roughly capable of restoring the order, the CNNSR (Fig. 11c) shows very good restoration of accuracy both overall and locally, in the vineyard rows. Figure 11e, f, g and h are zoom-ins of 11a, b, c and d, respectively.

It should be noted that while the PSNR is an acceptable figure of merit for evaluating SR algorithm performance when small details are only a minor portion of the image, it would be wise to estimate the PSNR locally (Mendelowitz et al. 2013), that is, in a ROI. Moreover, in agricultural monitoring, the accuracy of the measurements of some regions is more important than others, i.e., the accuracy in the measurements of vine rows (the black rows) is much more important than the accuracy of measuring the ground. Note that this applies to all typical row crops. The bicubic interpolation smears

the results whereas the CNNSR may sharpen them. This difference may be less important on average but in a small ROI, such as the red box in Fig. 11h, it can result in a very large error in temperature estimation.

To check this, the following numerical experiment was performed. The RMSE temperature was calculated in various areas inside the grapevine row. The vine temperature is significantly lower than the ground temperature. Thus, by thresholding the ground-truth image between 37.3 and 39.5 °C, a mask of pixels could be created that contained only the vine. The number of pixels decreases with temperature. This makes the estimation of upscaled performance more sensitive to mixed pixels due to smear caused by the estimator (bicubic or CNNSR). Indeed, as pixel numbers decreased, the RMSE of the bicubic interpolation increased from 0.3 to 0.85 °C relative to the ground truth. On the other hand, due to its sharp response, the RMSE of the CNNSR remained almost constant in the very low range of 0.011 °C to 0.038 °C relative to the ground truth, i.e., caused less mixed pixels. Similar to the RMSE results, the histogram intersections (H1; Eq. 4) of the two cases were compared. The H1 scores of the SR image relative to the ground truth image ranged from 0.82 to 0.66. The respective range for the bicubic interpolation image relative to the ground truth image was from 0.026 to 0.11, which is considerably lower than with the SR method.

To conclude, while CNNSR shows promising results with a better overall average PSNR, its potential advantage is even more salient when considering small ROIs.

End-to-end combined solution

To observe a field's spatial variability, image mosaicking is required. In this section, simulation results of an end-to-end algorithmic pipeline are presented, assuming that an aerial survey was performed with a low-cost thermal IR camera, along with drift correction, resolution improvement by CNNSR of each frame, and mosaicking of the corrected frames to a large mosaicked image of the field.

The mosaicked image, in this case, consisted of 3 strips, each composed of 8 pairs of images (Fig. 12). To mimic a high-altitude aerial survey, the images are downsampled by a factor of 2 from their ground truth. For the sake of mosaicking neighbors, images have 80.4% overlap.

The 24 images were jointly restored for their radiometric value by using the above joint estimation (minimization of Eq. 13). The resulting RMSE of the individual image is in the range of 1.4 °C to 1.7 °C. It is worth emphasizing that the large overlap between the images reduces the mutual information, and thus threatens the joint estimation. This was compensated for by enlarging the number of pairs used in the joint estimation from 8 to 24.

The next pipeline step is to double the spatial resolution of the restored images, using the CNNSR method. A few examples of the correction of vines' individual images from low resolution and thermal drift to radiometrically corrected with high resolution are presented in Fig. 13. Note that while the left image is sharp, the right image is sharper due to the improved resolution. The right image is also radiometrically corrected.

Following Eq. (5), mosaicked images were processed. The mosaicked image, composed of the corrected SR images, is presented in Fig. 14. The mosaicked image is continuous and clear. Compared to the ground-truth data, the RMSE is 0.83 °C. Note that the RMSE of the mosaicked image is better than the individual images' accuracy. This improved accuracy may be due to the averaging process embedded in the mosaicking process, and the noise-filtration process embedded in the CNNSR (Oz et al. 2020). For comparison, a mosaic image composed of the uncorrected low-resolution native images is presented in Fig. 15. Here, the averaging process embedded in the mosaicking process

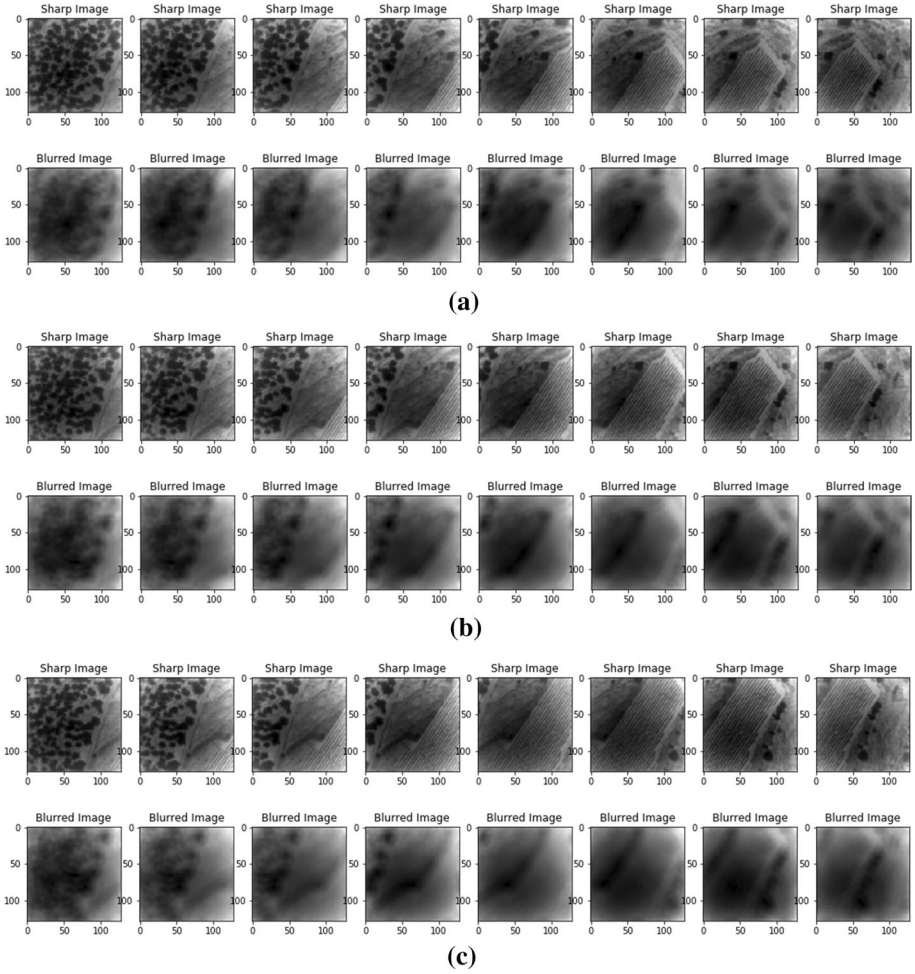

Fig. 12 Three strips of images. Each strip is composed of 8 pairs of images along the horizontal direction. Each pair includes a sharp and a blurred image. Every two adjacent strips have 80% overlap perpendicular to the strip direction. **a** First strip. **b** Second strip. **c** Third strip

failed to restore a correct value, resulting in the appearance of coarse squared artificial boundaries every ~ 25 pixels. By using bicubic interpolation with a factor of 2, the mosaic image is upscaled to the size of the ground-truth data. Compared to the ground-truth data, the RMSE is 8.251 °C, an order of magnitude larger than the result achieved with the proposed pipeline.

The accuracy of canopy temperature is critical for monitoring field variability. In previous work (Cohen et al. 2005; Ben-Gal et al. 2010), temperature differences between healthy plants and a stressed plant were shown to be limited to a narrow range of 2–4 °C. Thus, in the current example, the corrected data resulted in a sufficient temperature accuracy (Fig. 14) whereas the uncorrected data (Fig. 15) are unusable. Moreover, the improvement in the spatial resolution enables separating between the different vineyard rows, thus providing the capability of managing different zones in the field without the need for low flight height.

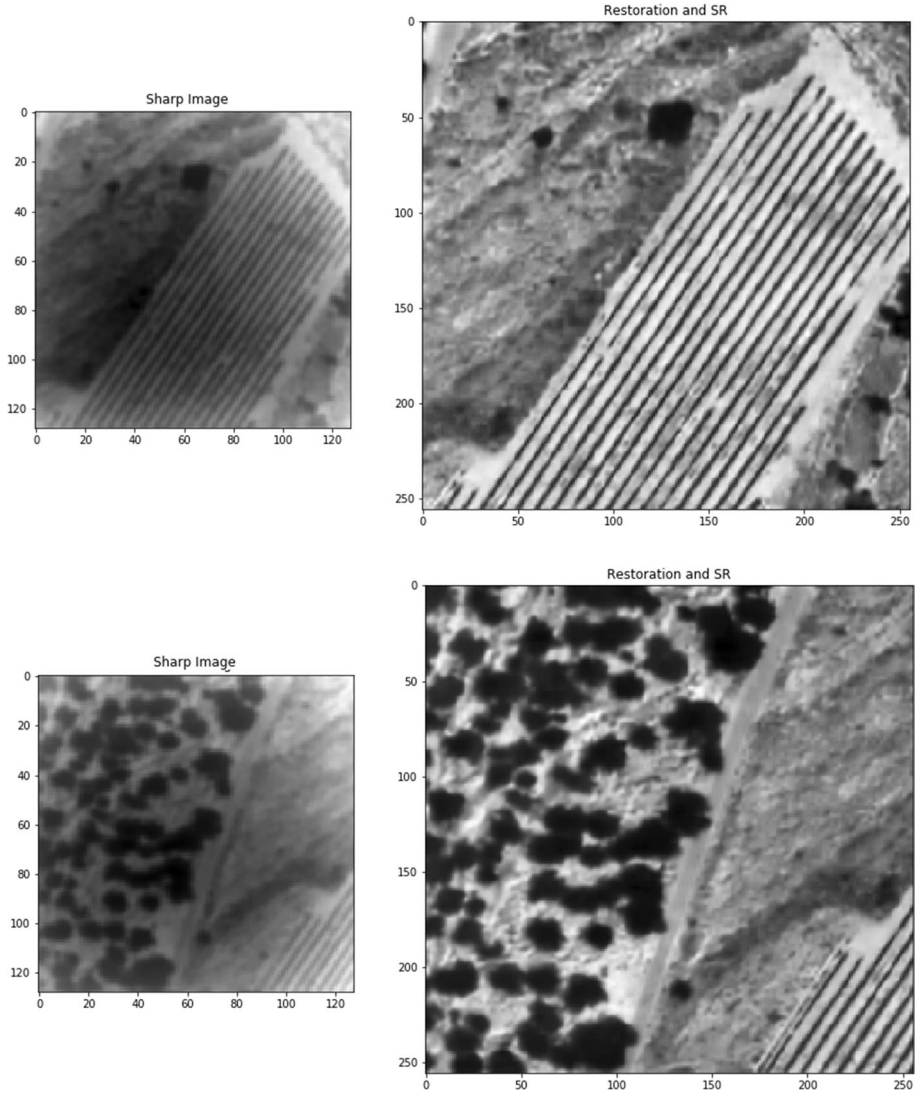

Fig. 13 Examples for the overall transformation. The native low-resolution image taken by an IR camera suffering from space-variant drift in gain and offset is given in the left column. The resulting image after radiometric correction and CNNSR is presented in the right column

Summary and conclusions

Agricultural crop fields are characterized by spatial variability. This variability needs to be monitored for high-resolution and high-accuracy information. Thermal longwave IR imaging has proven to be a useful tool for the remote sensing of various stresses in crops, mainly water status, in open agricultural fields. For the sake of accuracy, the thermal survey is performed with a high-cost radiometric camera. Resolution is obtained at the expense of FOV size. To cover the entire field, a mosaic image is produced,

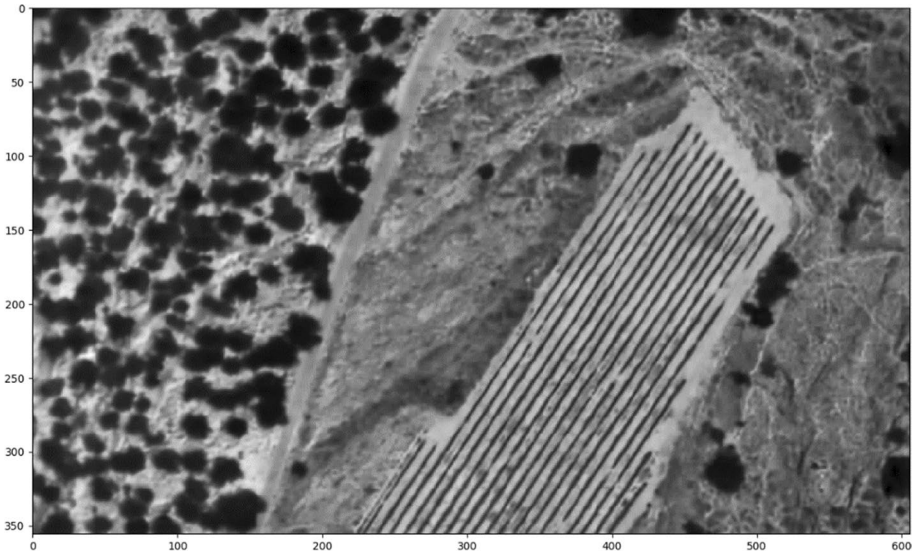

Fig. 14 Mosaic image composed of SR radiometrically corrected sub-images

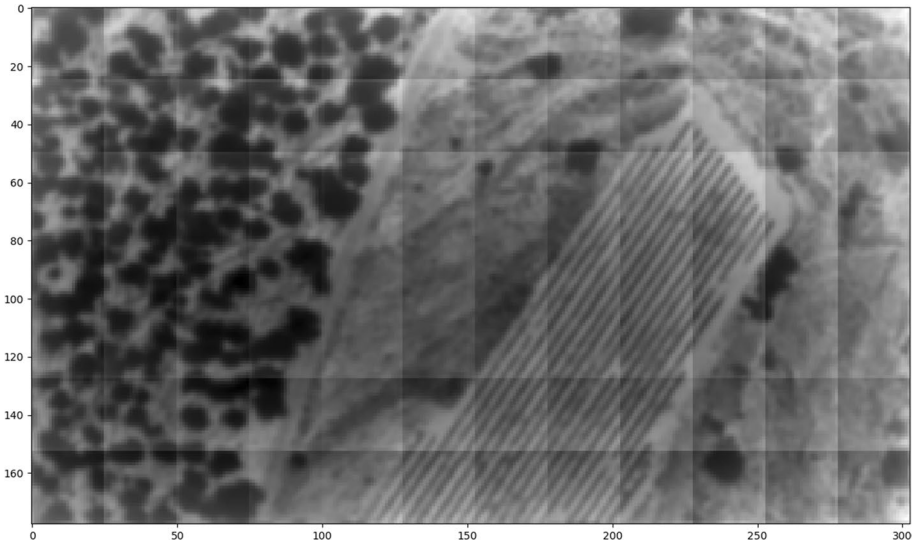

Fig. 15 Mosaic image composed of native low-resolution uncorrected images

composed of many smaller images taken by aerial survey. The high price and low spatial resolution of radiometric imaging are key technological barriers to the extensive implementation of IR remote sensing.

In this work, a three-stage pipeline algorithm relying on two computational imaging methods for radiometric image correction and SR methods, followed by a mosaicking

stage, was suggested to tackle these barriers. The methods were examined separately and in combination on agricultural data.

First, a joint estimation method was used to correct images taken by a thermal camera subjected to unknown drift of offset and gain. Tested on typical datasets from a vineyard, cotton field and peach orchard resulted in restoration of accuracy with RMSE in the range of 1.3 °C to 1.8 °C, using N = 9 pairs. Accuracy level was improved when the joint estimation was expanded to a larger aerial survey composed of 24 pairs of images, which narrowed the RMSE range to between 1.4 and 1.7 °C.

Preliminary results of the new CNNSR method were then provided, for the first time, on typical remotely sensed IR agricultural data. While not trained for the specific sensor, simulation results showed a promising advantage of the presented method over bicubic interpolation in × 2 upscaling, with an average gap of 1.8 db in the PSNR score of the overall image. The PSNR tended to be tolerated for the bicubic smear; indeed it was shown that when considering a ROI, the RMSE of the CNNSR is minor (0.03 °C); due to the mixed pixels associated with the bicubic interpolation, the RMSE was 0.85 °C in the same scenario. Similar results were obtained from the analysis of histogram similarity. When compared to the ground-truth data, while SR exhibited a minimal similarity of H1 = 0.66, the best similarity of the bicubic interpolation was H1 = 0.11. In addition, preliminary experimental results in × 4 upscaling showed promising potential for improvement over bicubic interpolation; compared to bicubic restoration, CNNSR showed a typical 50% improvement in restoration sharpness.

Finally, overall conceptual simulation results tied these two approaches, showing the benefits of the overall approach and for the first time, its potential contribution to mosaicking over an agricultural field. Results showed promising performance with a minimal RMSE of 0.8 °C for the mosaicked image, compared to a RMSE of 8.2 °C for mosaicked images without the proposed computational methods. The computational methods and the end-to-end approach yielded promising results, which under the discussed conditions, are essential for monitoring spatial variability of stress conditions in crops by remote sensing, using a relatively low-cost thermal camera from a high altitude.

Future prospects

Future work within the frame of this research might include continued development and training of the CNNSR method for the remote-sensing task and for other cameras. As concerns the joint estimation, a laboratory prototype camera with a controlled and low-hysteresis sequence of focus and defocus capabilities is under development. Preliminary results of mosaic images composed of SR images are under investigation. Major concerns associated with computation complexity and possible requirements are arising from model accuracy when measuring additional supportive information on the environment. Finally, high-accuracy plant thermography could also serve for close-range monitoring of plant growth.

Acknowledgements The authors would like to thank the Israeli Ministry of Agriculture's Kandel Program for funding this research under Grant No. 20-12-0030.

References

Alchanatis, V., Cohen, Y., Cohen, S., Möller, M., Sprinstin, M., Meron, M., et al. (2010). Evaluation of different approaches for estimating and mapping crop water status in cotton with thermal imaging. *Precision Agriculture, 11*, 27–41.

Ben-Gal, A., Kool, D., Agam, N., van Halsema, G. E., Yermiyahu, U., Yafe, A., et al. (2010). Whole-tree water balance and indicators for short-term drought stress in non-bearing 'Barnea' olives. *Agricultural Water Management, 98*, 124–133. https://doi.org/10.1016/j.agwat.2010.08.008.

Berni, J. A. J., Zarco-Tejada, P. J., Sepulcre-Canto, G., Fereres, E., & Villalobos, F. (2009). Mapping canopy conductance and CWSI in olive orchards using high resolution thermal remote sensing imagery. *Remote Sensing of Environment, 113*, 2380–2388.

Bhan, R. K., Saxena, R. S., Jalwania, C. R., & Lomash, S. K. (2009). Uncooled infrared microbolometer arrays and their characterisation techniques. *Defence Science Journal, 59*(6), 580–589.

Cohen, Y., Alchanatis, V., Meron, M., Saranga, Y., & Tsipris, J. (2005). Estimation of leaf water potential by thermal imagery and spatial analysis. *Journal of Experimental Botany, 56*(417), 1843–1852.

Cohen, Y., Alchanatis, V., Prigojin, A., Levi, A., & Soroker, V. (2012). Use of aerial thermal imaging to estimate water status of palm trees. *Precision Agriculture*. https://doi.org/10.1007/s11119-011-9232-7.

Costa, J. M., Grant, O. M., & Chaves, M. M. (2013). Thermography to explore plant–environment interactions. *Journal of Experimental Botany, 64*(13), 3937–3949.

Dong, C., Loy, C. C., He, K., & Tang, X. (2014). Learning a deep convolutional network for image super-resolution. In D. Fleet, T. Pajdla, B. Schiele, & T. Tuytelaars (Eds.), *Computer vision—ECCV 2014. ECCV 2014. Lecture notes in computer science* (Vol 8692, pp. 184–199). Cham: Springer.

Ehrler, W. L. (1973). Cotton leaf temperatures as related to soil water depletion and meteorological factors. *Agronomy Journal, 65*, 404–409.

Elad, M., & Feuer, A. (1997). Restoration of a single super-resolution image from several blurred, noisy, and undersampled measured images. *IEEE Transactions on Image Processing, 6*, 1646–1658.

Farsiu, S., Dirk Robinson, M., Elad, M., & Milanfar, P. (2004). Fast and robust multiframe super resolution. *IEEE Transactions on Image Processing, 13*, 1327–1343.

Gates, D. M. (1964). Leaf temperature and transpiration. *Agronomy Journal, 56*, 273–277.

Grant, O. M., Tronina, L., Jones, H. G., & Chaves, M. M. (2007). Exploring thermal imaging variables for the detection of stress responses in grapevine under different irrigation regimes. *Journal of Experimental Botany, 58*, 815–825.

Holman, J. P. (1989). *Heat transfer*. Boston: McGraw Hill.

Jia, W., Zhang, H., He, X., & Wu, Q. (2006). A comparison on histogram based image matching methods. In *2006 IEEE International Conference on Video and Signal Based Surveillance*, Sydney, Australia (pp. 97–97). https://doi.org/10.1109/AVSS.2006.5

Jones, H. G. (1994). *Plant and microclimate* (2nd ed.). Cambridge, UK: Cambridge University Press.

Kim, J., Lee, J. K., & Lee, K. M. (2016). Accurate image super-resolution using very deep convolutional networks. In *2016 IEEE Conference on Computer Vision and Pattern Recognition (CVPR)*. https://doi.org/10.1109/CVPR.2016.182

Klapp, I., Brand, O., Yafin, P., Papini, S., Oz, N., Bahat, I., et al. (2019). Using computational optics for agricultural monitoring with an emphasis on irrigation management zones. In J. V. Stafford (Ed.), *Precision agriculture '19*. Wageningen: Wageningen Academic Publishers. https://doi.org/10.3920/978-90-8686-888-9_82

Klapp, I., Papini, S., & Sochen, N. (2017). Radiometric imaging by double exposure and gain calibration. *Applied Optics, 56*, 5639–5647.

Kopeika, N. S. (1998). *A system engineering approach to imaging*. Bellingham, WA: SPIE Optical Engineering Press.

Kusnierek, K., & Korsaeth, A. (2014). Challenges in using an analog uncooled microbolometer thermal camera to measure crop temperature. *International Journal of Agricultural and Biological Engineering, 7*, 60–74.

LSQR (2018). Sparse Equations and Least Squares. Retrieved September 15, 2020, from https://web.stanford.edu/group/SOL/software/lsqr/.

Mandanici, E., Tavasci, L., Corsini, F., & Gandolfi, S. (2019). A multi-image super-resolution algorithm applied to thermal imagery. *Applied Geomatics, 11*, 215–228.

Manickavasagan, A., Digvir, J. S., White, N. D. G., & Paliwal, J. (2005). Applications of thermal imaging in agriculture—a review. In: *CSAE/SCGR 2005 Meeting*, Paper No. 05–002. Retrieved September 15, 2020, from https://www.csbe-scgab.ca/docs/meetings/2005/05-002.pdf.

Mendelowitz, S., Klapp, I., & Mendlovic, D. (2013). Design of an image restoration algorithm for the TOMBO imaging system. *Journal of the Optical Society of America A, 30*, 1193–1204.

Nugent, P. W., & Shaw, J. A. (2014). Calibration of uncooled LWIR microbolometer imagers to enable long-term field deployment. In: *Proceedings*, *Infrared imaging systems: design, analysis, modeling, and testing* XXV (Vol 9071, p. 90710V). https://doi.org/10.1117/12.2053082

Oz, N., Sochen, N., & Klapp, I. (2020). Rapid super resolution for infrared imagery. *Optics Express*. https://doi.org/10.1364/OE.389926.

Papini, S., Yafin, P., Klapp, I., & Sochen, N. (2018). Joint estimation of unknown radiometric data, gain and offset from thermal images. *Applied Optics, 57*, 10390–10401.
Petrović, I., Marjanović, M., Ćosić, M., Savić, S., & Cvijanović, S. (2016). Infra-red thermography for detecting drought in agriculture crops and scheduling irrigation. *Economics of Agriculture, 2*, 461–469.
Rivenson, Y., Göröcs, Z., Günaydin, H., Zhang, Y., Wang, H., & Ozcan, A. (2017). Deep learning microscopy. *Optica, 4*(11), 1437–1443.
Sun, J., Xu, Z., & Shum, H.-Y. (2008). Image super-resolution using gradient profile prior. In *2008 IEEE Conference on Computer Vision and Pattern Recognition*. https://doi.org/10.1109/CVPR.2008.4587659
Tanner, C. B. (1963). Plant temperatures. *Agronomy Journal, 55*, 210–211.
Tempelhahn, A., Budzier, H., Krause, V., & Gerlach, G. (2016). Shutter-less calibration of uncooled infrared cameras. *Journal of Sensors and Sensor Systems, 5*, 916.
Tilling, K., O'Leary, G. J., Ferwerda, J. G., Jones, S. D., Fitzgerald, G. J., Rodriguez, D., et al. (2007). Remote sensing of nitrogen and water stress in wheat. *Field Crops Research, 104*, 77–85.
United Nations (2017). *Water for sustainable food and agriculture*. Rome: FAO, ISBN 978-92-5-109977-3
Vidal, D., & Pitarma, R. (2019). Infrared thermography applied to tree health assessment: A review. *Agriculture, 9*(7), 156. https://doi.org/10.3390/agriculture9070156.
Zhou, J., Kwan, C., & Budavari, B. (2016). Hyperspectral image super-resolution: A hybrid color mapping approach. *Journal of Applied Remote Sensing*. https://doi.org/10.1117/1.JRS.10.035024.

Affiliations

Iftach Klapp[1] · Peretz Yafin[1,2] · Navot Oz[1,3] · Omri Brand[1,4] · Idan Bahat[1,5] · Eitan Goldshtein[1] · Yafit Cohen[1] · Victor Alchanatis[1] · Nir Sochen[4]

1 Institute of Agricultural Engineering, Agricultural Research Organization, Volcani Center, Rishon LeZion, Israel

2 Department of Computer Science, Tel Aviv University, 69978 Tel Aviv, Israel

3 School of Electrical Engineering, Tel Aviv University, 69978 Tel Aviv, Israel

4 Department of Mathematics, Tel Aviv University, 69978 Tel Aviv, Israel

5 The Robert H. Smith Institute of Plant Sciences and Genetics in Agriculture, Faculty of Agriculture, Food and Environment, The Hebrew University of Jerusalem, 76100 Rehovot, Israel